Analysis of Impedance Tuning Control and Synchronous Switching Technique for a Semibridgeless Active Rectifier in Inductive Power Transfer Systems for Electric Vehicles

Sangjoon Ann, *Student Member, IEEE*, and Byoung Kuk Lee, *Senior Member, IEEE*

***Abstract*—In inductive power transfer (IPT) systems, load, and magnetic coupling variations cause an impedance mismatch. Impedance mismatch is one of the most serious problems in IPT systems for electric vehicles (EVs) because an EV is not always parked in the same location. Therefore, an impedance tuning control for semibridgeless active rectifiers (SBARs) is proposed in this article to compensate for this mismatch. The proposed impedance tuning control is achieved by adjusting the turn-ON point and duty of the SBAR without using any additional component. Moreover, a technique for detecting the voltage-rising edge of the SBAR switch is proposed to extract the switching frequency and to synchronize the SBAR with the primary system. A 3.3-kW prototype of the IPT system with the SBAR is manufactured, and the proposed impedance tuning control is verified through experimental results according to the coupling coefficient. The proposed control can achieve an efficiency improvement of 6.4% under the impedance mismatch.**

***Index Terms*—Electric vehicle (EV), impedance mismatch, impedance tuning control, inductive power transfer (IPT), wireless power transfer (WPT).**

I. Introduction

INDUCTIVE power transfer (IPT) is a promising technology for various industrial applications because of its technical advantages and convenience. In particular, IPT technology for electric vehicle (EV) applications makes it possible to park and charge the EV simultaneously because the power is transferred without any physical contact [1]–[3]. As primary and secondary IPT systems are physically separated, the distance between IPT pads varies with the parking position of the EV [3]. Therefore, SAE standards, which are the IPT charging standards for EVs, recommend that the IPT system should be designed considering the misalignment tolerance between the IPT pads [4]. Variations in the primary and secondary inductances must be considered to comply with the design recommended by SAE standards because the inductances are directly related to the distance between the IPT pads. Generally, in the IPT system, the variations in inductance are dealt with by tuning a resonant network as an input impedance of the network remains inductive. The typical tuning methods can be employed to deal with a small range of inductance variations. However, in the EV applications, the inductance variations are wider because SAE standards also recommend using an aluminum (Al) shield over the secondary IPT pad to protect human and electronic devices from magnetic flux [4], [5]. As shown in Fig. 1, when the misalignment tolerance and Al shield are both considered, the primary and secondary inductances change significantly because the Al shield has a low permeability and interferes with the transmission of the magnetic flux [3]–[5]. Consequently, the IPT system cannot operate at the designed resonant frequency because the inductance variations cause an impedance mismatch in the primary and secondary resonant networks. In addition, in the IPT system, an optimal load impedance is different for the different parking positions and output power levels. Therefore, the impedance mismatch caused by the misalignment and the output power levels results in a decrease in the power transfer efficiency and an inability to obtain the desired output voltage gain [6]–[18].

Several recent studies have examined methods for solving the problem of impedance mismatch compensation. The compensation methods are largely divided into two types: the methods of adjusting the resonant capacitance [6]–[13] and the methods of adjusting the load equivalent impedance [14]–[18].

To adjust the resonant capacitance, a switched capacitor (SC) methods using switches and discrete capacitors has been introduced in [6]–[9]. However, the volume and cost of the system increase in the SC method because numerous switches and capacitors are required for fine-tuning. To reduce the number of components, controllable capacitor methods have been

Manuscript received June 25, 2020; revised November 10, 2020; accepted December 25, 2020. Date of publication January 6, 2021; date of current version May 5, 2021. This work was supported in part by the National Research Foundation of Korea (NRF) grant funded by the Korea Government (MSIT) (2020R1A2C2003445), in part by the Korea Institute of Energy Technology Evaluation and Planning (KETEP), and in part by the Ministry of Trade, Industry, and Energy (MOTIE) of the Republic of Korea (2018201010650A). This paper was presented in part at the IEEE Applied Power Electronics Conference and Exposition, New Orleans, LA, USA, March 15–19, 2020. Recommended for publication by Associate Editor U. K. Madawala. *(Corresponding author: Byoung Kuk Lee.)*

Sangjoon Ann is with the Department of Electrical and Computer Engineering, Sungkyunkwan University, Suwon 16419, South Korea (e-mail: ahnsjoon@skku.edu).

Byoung Kuk Lee is with the College of Information and Communication Engineering, Sungkyunkwan University, Suwon 16419, South Korea (e-mail: bkleeskku@skku.edu).

Color versions of one or more figures in this article are available at https://doi.org/10.1109/TPEL.2021.3049546

Digital Object Identifier 10.1109/TPEL.2021.3049546

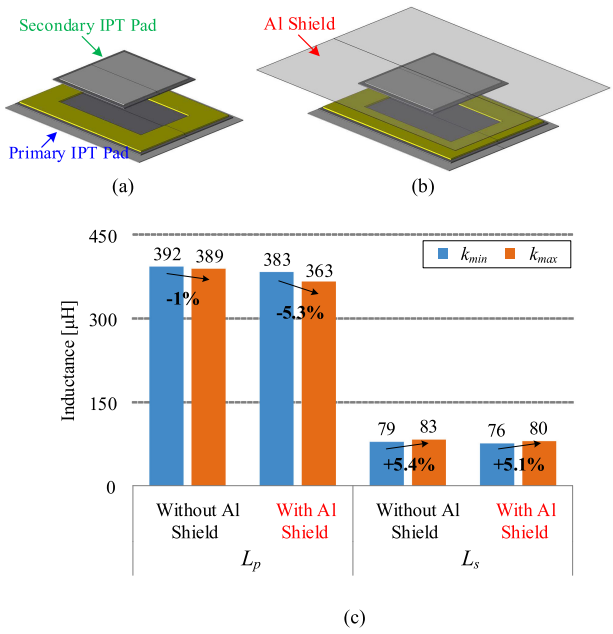

Fig. 1. Finite element analysis simulation results according to Al shield. (a) IPT pads without Al shield. (b) IPT pads with Al shield. (c) Variations in the primary inductance L_p and secondary inductance L_s.

proposed [10]–[13]. Tuning capacitors with a buck converter and a fixed-frequency unidirectional switch push-pull converter (USPP) have been proposed [10]. The USPP can finely adjust the capacitance using fewer components to maintain a constant primary current under both inductively and capacitively mistuned conditions [10]. Other fine-tuning methods include a pulsewidth modulation (PWM)-controlled capacitor [11] and a voltage-controlled capacitor [12]. In [11], the capacitance of the tuning capacitor is controlled using a PWM-controlled switch, which is connected to the tuning capacitor in series. In [12] and [13], the capacitances are finely tuned using an analog multiplier or a high-resolution stepper motor, respectively.

To adjust load equivalent impedance, a boost active bridge based secondary IPT system is proposed to achieve high efficiency by tuning the load impedance [14]. In [15], an auxiliary measurement coil and decoupling transformer in an IPT system with an active rectifier have been studied to achieve high efficiency under reactance mismatch conditions and the variations in load. However, these methods also have volume- and cost-related problems because of the additional components; hence, the power density is inevitably reduced.

To improve the power density, control strategies for the active rectifiers without additional components have been studied [16]–[18]. In [16], a fixed-frequency phase-shift control for a secondary semibridgeless active rectifier (SBAR) in a multiple-pickup IPT system has been proposed. The SBAR in [16] could control the output voltage gain without changing the primary control parameters. Thus, each secondary circuit could be independently controlled, and communication between the primary and secondary systems is not required. In [17], a fixed-frequency triple phase shift (TPS) control for a bidirectional IPT system has been proposed. The TPS control can achieve load matching and zero-voltage switching (ZVS) on the primary and secondary systems [17]. However, the systems in [16] and [17] suffers from two major disadvantages which make it difficult to use in an EV application. First, the fixed-frequency control has a limitation regarding compensation under a large range of misalignment and a wide range of load variations. Second, the value of the fixed frequency must be determined with a sufficient margin to ensure that the system operates in the ZVS region even if a large impedance mismatch occurs. This indicates that the fixed-frequency control cannot minimize the primary VA rating, and variable frequency control is required. To apply the variable-frequency control to the primary and secondary IPT systems, a synchronous switching technique is also required.

To achieve high efficiency under the large misalignment and the wide variations in load, a variable-frequency TPS control has been proposed [18]. Four variables are controlled to compensate for the wide range of the impedance mismatch while achieving ZVS on both side converters. However, a mutual inductance M has to be estimated by looking up an impedance map at startup. Moreover, the primary phase shift angle and operating frequency are controlled according to a lookup table using the estimated M and a wirelessly fed back output power. The use of the impedance map and lookup table can ease the amount of computation of a digital controller, but many premeasured data points are required to achieve precise control. In addition, it is difficult to deal with changes in operating conditions because the lookup table cannot be updated during charging.

Therefore, in this article, a variable-frequency impedance tuning control and a synchronous switching technique for an SBAR of the secondary IPT system are proposed. The proposed control can compensate for the wide range of the impedance mismatch and allow fine-tuning by controlling the output equivalent impedance inductively or capacitively with respect to the coupling coefficient and output power conditions. The operating frequency of the primary system is controlled to track the zero-phase angle (ZPA) frequency for minimizing the VA rating [19] and to achieve the wide range of impedance mismatch compensation. The secondary SBAR can be synchronized with the primary system using the proposed synchronous switching technique with minimal information from the primary system. The proposed control has the following advantages.

1) The operating range is expanded under misalignment conditions because a primary-side variable-frequency control and a secondary-side impedance tuning control are both applied.
2) The operating frequency for the primary and secondary system is determined in real time without an impedance map or a lookup table.
3) Additional component is not required.

The remainder of this article is organized as follows. In Section II, the system configuration and specifications are presented. In Section III, the design of the resonant network and the proposed control has been analyzed. The synchronous switching technique and the frequency extraction method for the secondary SBAR are proposed in Section IV. Finally, in Section V, the proposed impedance tuning control and the synchronous switching technique are verified through experimental results.

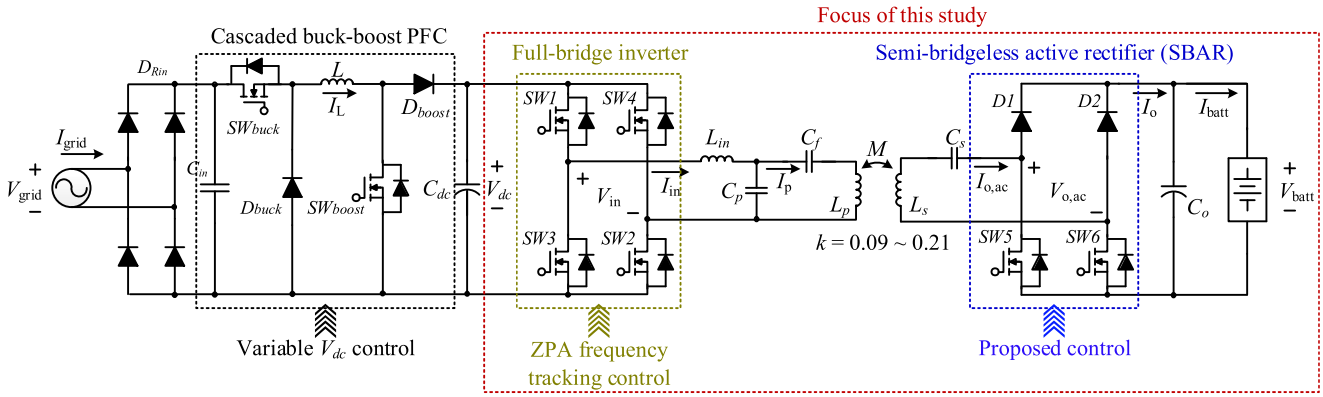

Fig. 2. A 3.3-kW IPT system with SBAR.

TABLE I
SPECIFICATIONS OF IPT SYSTEM

Parameter	Value	[Unit]
DC link voltage V_{dc}	200–420	[V]
Battery voltage V_{batt}	240–410	[V]
Rated output power P_o	3.3	[kW]
Switching frequency f_{sw}	81.38-90	[kHz]
Nominal frequency f_{nom}	85	[kHz]
Coupling coefficient k	0.09~0.21	-

II. System Configuration

Fig. 2 shows a 3.3-kW IPT system with an SBAR. The specifications and parameters of the system are listed in Table I. As shown in Fig. 2, on the primary side, a full-bridge inverter supplies an ac voltage to the resonant network from the dc-link voltage V_{dc}, and a ZPA frequency tracking control is applied to the inverter for minimizing VA rating [19]. On the secondary side, an ac–dc converter is used for the SBAR, and the proposed impedance tuning control is applied.

In an EV application, a change in the parking position of the EV causes variations in the coupling coefficient k, which are directly related to output voltage variations. Moreover, a high-voltage battery pack for EVs has a wide range of terminal voltage which varies with the state of charge. This indicates that the IPT system with the SBAR must be operable over a wide range of both k and the output voltage. If the dc-link voltage is controlled as a fixed value, the SBAR is the only means to control the output voltage in the system because the primary full-bridge inverter is controlled by the ZPA frequency tracking control. It should be noted that the ZPA frequency tracking control is not used for the control of the output voltage but for minimizing the VA rating. This indicates that the duty ratio of the SBAR should be excessively increased to obtain the maximum output voltage under the lowest-k condition. If the SBAR operates with a high duty ratio, a large conduction loss occurs, reducing the system efficiency. Therefore, a variable dc-link voltage is adopted in this article, and the dc-link voltage range is designed considering the variation in k and the power factor of a cascaded buck-boost power factor correction converter [20].

The primary and secondary resonant networks are essential in the IPT system because the loosely coupled IPT coils have large leakage inductances [2]. The output characteristics of the resonant network must be considered when designing the IPT system with the SBAR because they are directly related to the output characteristics of the SBAR. If the resonant network has a constant-current (CC) output characteristic, the SBAR operates as a step-down-type converter [16]. In contrast, with a constant-voltage (CV) resonant network, the SBAR operates as a step-up-type converter [21]. In this article, the primary *LCC* network and the secondary series network are adopted to obtain the CV output characteristics regardless of load variation [19]. Therefore, the SBAR operates as a step-up-type converter with the LCC-S network. The primary *LCC* network also has a low possibility of bifurcation because of a large parallel capacitance C_p [19]. The design procedure for the resonant network and the analysis of the proposed control will be described in the following section by considering the impedance mismatch.

III. Analysis of Proposed Impedance Tuning Control

A. Measurement of Parameter Variation

To design the resonant network, it is necessary to consider the variations in IPT coil parameters according to the parking position. The IPT coil parameters are represented by L_p, L_s, and k, as shown in Fig. 2. L_p and L_s are the inductances of the primary and secondary IPT coils, respectively. The physical distance between the primary and secondary pads changes according to the parking position, which is represented by the change in L_p, L_s, and k. To measure the change in the IPT coil parameters, the primary and secondary pads are manufactured based on SAE standards, as shown in Fig. 3. The number of turns of the primary pad is designed considering the primary pad current to be below 20 A [19], and the number of turns of the secondary pad is designed considering the secondary quality factor to reduce the occurrence of bifurcation [22]. It should be noted that the Al shield shown in Fig. 3(a) is placed over the secondary IPT pad when measuring the IPT coil parameters. Table II shows the IPT coil parameters which are measured according to the coil-to-coil vertical gap and horizontal misalignment, and Fig. 4 shows the contour plots of the magnetic flux density according

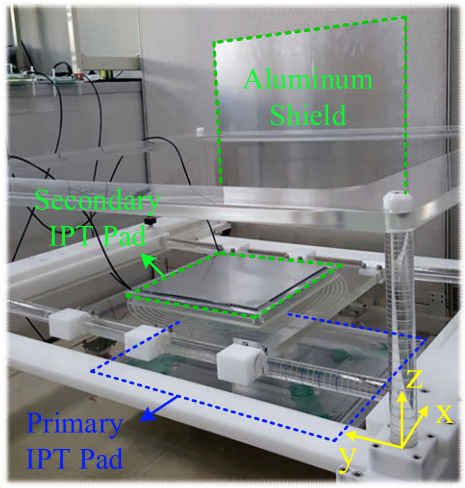

(a)

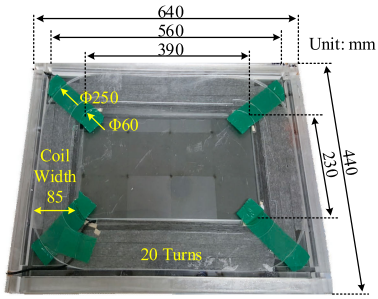

(b)

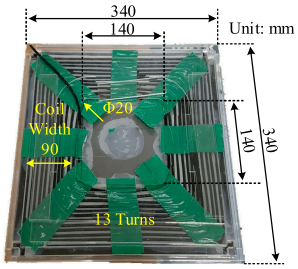

(c)

Fig. 3. A 3.3-kW IPT pad structure. (a) Total pad structure. (b) Primary IPT pad. (c) Secondary IPT pad.

TABLE II
MEASURED PARAMETER VARIATIONS OF IPT COILS ACCORDING TO K

Parameter	k_{min} = 0.09	k_{max} = 0.21	[Unit]
x	75	0	[mm]
y	100	75	[mm]
z	170	100	[mm]
L_p (20 turns)	460.6	441.1	[μH]
L_s (13 turns)	77.11	80.07	[μH]

to k, obtained via finite element analysis. Note that the vertical gap, which is also called z-axis gap, is between 100 and 170 mm. The range of the horizontal misalignment, which is also called the x and y axes misalignment, is from $x/y = 0/0$ mm to $x/y = \pm 75/100$ mm. The directions of the vertical gap and horizontal misalignment are depicted in Fig. 5 [4]. As shown in Table II,

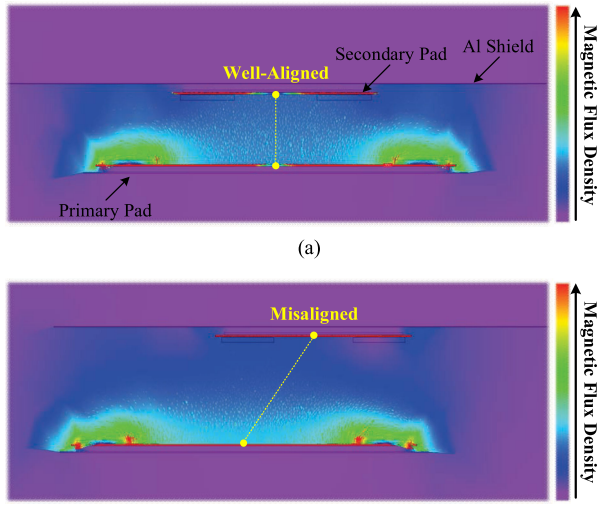

(a)

(b)

Fig. 4. Contour plot of magnetic flux density according to the change in parking position. (a) Well-aligned parking ($k = k_{\max}$). (b) Misaligned parking ($k = k_{\min}$).

Fig. 5. Directions of the vertical gap and horizontal misalignment.

L_p decreases and L_s increases when k increases. In contrast, when k decreases, L_p increases and L_s decreases. The decrease in L_p when the IPT pads become close to each other is because the large Al shield on the secondary side approaches the primary pad and interferes with the transmission of the magnetic flux. On the other hand, the increase in L_s when the pads become close to each other is because the large primary ferrite core assists the transmission of the magnetic flux as the primary ferrite core approaches the secondary IPT pad. These inductance variations cause the impedance mismatch because the capacitances in the resonant network are fixed, regardless of the change in k.

B. Design of Resonant Network

The resonant network must be designed with specific values of L_p, L_s, and k for a specific parking position. This position is defined as a design point in this article. The resonant components of the network at the design point are designed at a nominal resonant frequency f_{nom} of 85 kHz [4]. Generally, the minimum coupling coefficient $k_{\min}$ is selected as the design point in an IPT system [19]. The minimum output voltage is designed at $k = k_{\min}$ because this is the worst condition in terms of wireless power transfer. In the case of the LCC-S network, the output voltage of the network increases as k increases [19]. The voltage cancellation control is applied to limit the increase in the output voltage at $k = k_{\max}$ [19].

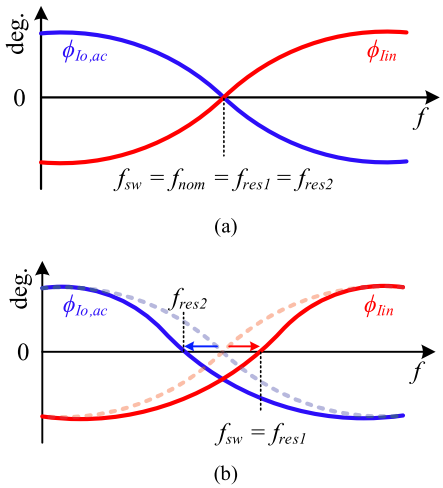

Fig. 6. Phase angles of I_{in} and $I_{o,ac}$ according to k conditions. (a) Design point ($k = k_{\min}$). (b) Impedance mismatch at $k = k_{\max}$.

As $k_{\min}$ is selected as the design point, the impedance mismatch occurs in the well-aligned parking condition. In other words, as k increases from the design point, $f_{\text{res}1}$ increases, and the secondary resonant frequency $f_{\text{res}2}$ decreases. Table II shows the measured L_p, L_s, and the resonant frequencies at $k = k_{\min}$ and $k_{\max}$. The impedance mismatch appears as a change in not only the inductances but also the phase angles of the input current I_{in} and the output ac current $I_{o,ac}$, as shown in Fig. 6. When the system operates at the design point, the phase angles of I_{in} and $I_{o,ac}$ are identical and zero, as shown in Fig. 6(a). However, as k increases, the zero-crossing points of the curves are separated because of the impedance mismatch, as shown in Fig. 6(b). Note that the reference for the phase angles of I_{in} and $I_{o,ac}$ is the input voltage V_{in}.

C. Principle of Proposed Impedance Tuning

As shown in Fig. 6(b), $f_{\text{res}1}$ and $f_{\text{res}2}$ are separated because an impedance mismatch occurs because of the change in L_p and L_s. Under the mismatch condition, the system operates at $f_{\text{res}1}$ because the primary inverter is controlled to track the ZPA frequency. However, as $f_{\text{res}1}$ is not equal to $f_{\text{res}2}$, the power transfer efficiency decreases, and the system cannot obtain the desired voltage gain. Hence, the objective of the proposed control is to control the SBAR so that $f_{\text{res}1}$ and $f_{\text{res}2}$ are the same even when k changes from the design point.

The basic principle of the proposed control is to compensate for the impedance mismatch by controlling the equivalent output impedance $Z_{o,ac}$ inductively or capacitively. A detailed method for implementing inductive or capacitive $Z_{o,ac}$ by controlling the SBAR is described in the following section. As shown in Fig. 7, if $Z_{o,ac}$ is capacitively controlled, it is equivalent to connecting an additional capacitance C_{add} in series with the secondary network, so that the secondary equivalent impedance Z_{22} also becomes capacitive because Z_{22} is represented by (1)

$$Z_{22} = j\omega L_s + \frac{1}{j\omega C_s} + Z_{o,ac}. \tag{1}$$

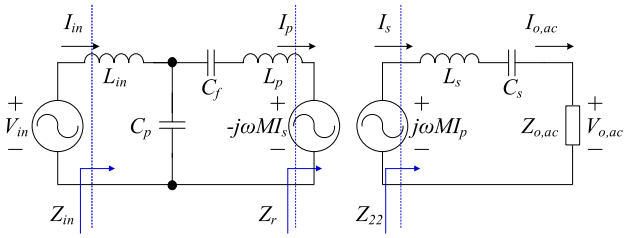

Fig. 7. Equivalent circuit of the LCC-S resonant network.

Because of C_{add}, $f_{\text{res}2}$ increases, as shown in (2)

$$f_{\text{res}2} = \left.\frac{1}{2\pi\sqrt{L_s\left(C_s \parallel C_f\right)}}\right|_{\text{Capacitive } Z_{o,ac}}. \tag{2}$$

The primary reflected impedance Z_r is represented by (3), and Z_r becomes inductive because of the capacitive Z_{22}

$$Z_r = \frac{\omega^2 M^2}{Z_{22}}. \tag{3}$$

When Z_r becomes inductive, $f_{\text{res}1}$ decreases, as shown in (4), because it is equivalent to connecting an additional inductor L_{add} in series with L_p. Consequently, if $Z_{o,ac}$ is capacitively controlled, it is possible to compensate for the impedance mismatch due to the increase in k

$$f_{\text{res}1} = \left.\frac{1}{2\pi\sqrt{\left(L_p + L_{\text{add}}\right)\left(C_p \parallel C_f\right)}}\right|_{\text{Capacitive } Z_{o,ac}}. \tag{4}$$

In contrast, if $Z_{o,ac}$ is inductively controlled, it is equivalent to connecting L_{add} in series on the secondary side and C_{add} in series on the primary side. Therefore, as shown in (5) and (6), $f_{\text{res}1}$ increases, and $f_{\text{res}2}$ decreases

$$f_{\text{res}1} = \left.\frac{1}{2\pi\sqrt{L_p\left(C_p \parallel C_f \parallel C_{\text{add}}\right)}}\right|_{\text{Inductive } Z_{o,ac}} \tag{5}$$

$$f_{\text{res}2} = \left.\frac{1}{2\pi\sqrt{\left(L_s + L_{\text{add}}\right)C_s}}\right|_{\text{Inductive } Z_{o,ac}}. \tag{6}$$

In this article, changes in k appear with an increasing trend from $k = k_{\min}$ because the resonant network is designed at $k_{\min}$. Therefore, $Z_{o,ac}$ must be capacitively controlled when the impedance mismatch occurs because of the increase in k.

To extend the proposed control to differently-tuned secondary networks, the magnitude and phase of Z_{22} are analyzed according to the change in $Z_{o,ac}$. It should be noted that $Z_{o,ac}$ is represented by the complex summation of the load equivalent resistance $R_{o,ac}$ and the load equivalent reactance $X_{o,ac}$. As shown in Fig. 8, the phase of Z_{22} is changed along one trajectory according to $X_{o,ac}$ in each network, and the trend is maintained under the variations in $R_{o,ac}$. Therefore, it is proved that the impedance analysis in this article can be extended to the differently-tuned secondary networks, such as parallel and *LCL* networks.

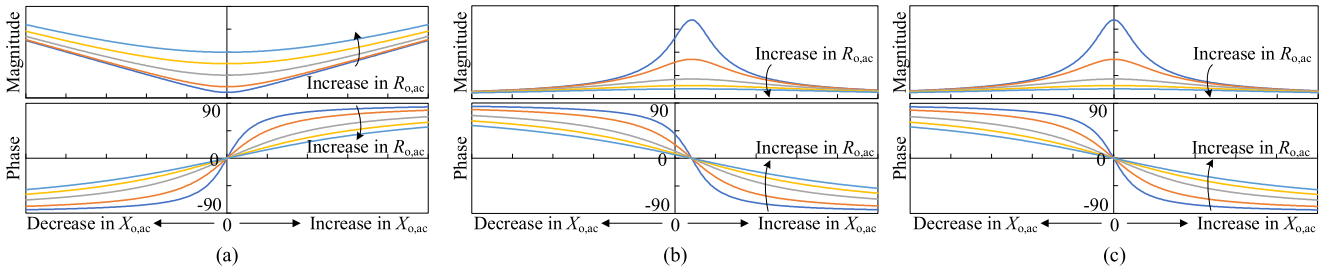

Fig. 8. Magnitude and phase of Z_{22} according to $Z_{o,ac}$ in differently tuned secondary resonant networks. (a) Series. (b) Parallel. (c) *LCL*.

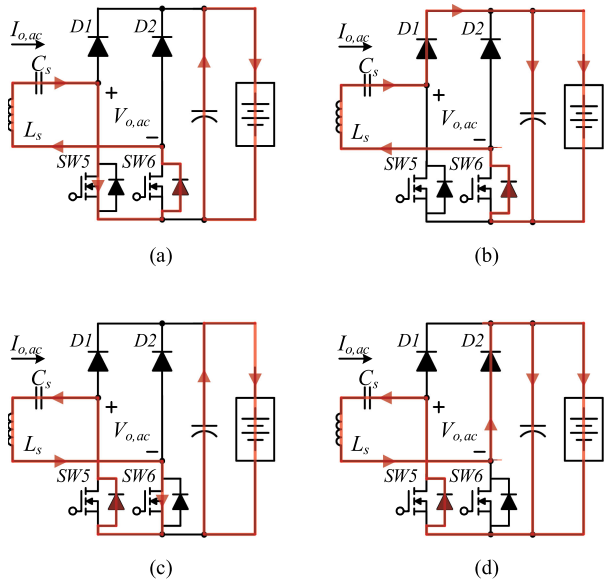

Fig. 9. Operation modes according to the switching state of SBAR. (a) SW5 turned ON ($I_{o,ac} > 0$). (b) SW5 turned OFF ($I_{o,ac} > 0$). (c) SW6 turned ON ($I_{o,ac} < 0$). (d) SW6 turned OFF ($I_{o,ac} < 0$).

D. Analysis of Proposed Impedance Tuning

Fig. 9 shows the operation modes according to the switching states of the SBAR. As shown in Fig. 9(a) and (c), the output ac voltage $V_{o,ac}$ becomes zero if SW5 or SW6 is turned ON when $I_{o,ac} > 0$ or $I_{o,ac} < 0$, respectively. When all the switches are turned OFF, the SBAR operates as a typical diode rectifier, as shown in Fig. 9(b) and (d). Therefore, it is possible to control the shape of $V_{o,ac}$ by controlling the switching states of the SBAR. Controlling the shape of $V_{o,ac}$ changes the fundamental wave component of the output ac voltage $V_{o,ac1}$, and hence, $Z_{o,ac}$ can be controlled, as follows:

$$Z_{o,ac} = \frac{V_{o,ac1}}{I_{o,ac1}}. \tag{7}$$

The shape of $V_{o,ac}$ is controlled by adjusting the turn-ON point and duty of the SBAR to implement the proposed impedance tuning. In Fig. 10, the control parameters are defined for the analysis of the proposed control. α is defined as the turn-ON point at which the switch of the SBAR is turned ON. β is the duty of the SBAR switches. γ, which is also a turn-ON point, is similar to α, but γ is defined as an angle from the beginning of the positive half-cycle of $V_{o,ac}$ to the mid-point of β. Note that α is defined for mathematical interpretation, and γ is defined for control on the secondary side. The reference point of γ is $\gamma = 90°$, and $Z_{o,ac}$ is resistive at this point. In this article, the state where only the duty is controlled because γ is maintained 90° is defined as β control.

When the proposed control is applied to the SBAR, $V_{o,ac1}$ is derived using Fourier series, as follows:

$$V_{o,ac1} = a_1 \cos \omega t + b_1 \sin \omega t \tag{8}$$

$$a_1 = \frac{2V_{\text{batt}}}{\pi} \left\{ \sin \alpha - \sin (\alpha + \beta) + 2 \sin \phi_{I_{o,ac}} \right\} \tag{9}$$

$$b_1 = \frac{2V_{\text{batt}}}{\pi} \left\{ \sin \alpha - \cos (\alpha + \beta) + 2 \cos \phi_{I_{o,ac}} \right\}. \tag{10}$$

In this analysis, it is assumed that only the fundamental wave components of $V_{o,ac}$ and $I_{o,ac}$ are involved in active power transmission. Thus, the magnitude of $I_{o,ac1}$ can be derived using the magnitude of $V_{o,ac1}$ and the output power as follows:

$$I_{o,ac1} = \frac{P_o}{V_{o,ac1}} \tag{11}$$

Subsequently, $Z_{o,ac}$, Z_{22}, and Z_r can be derived using (7), (1), and (3), respectively. As shown in Fig. 7, the input impedance Z_{in} is represented by the following:

$$Z_{in} = \frac{1}{\frac{1}{j\omega L_p + \frac{1}{j\omega C_f} + Z_r} j\omega C_p} + j\omega L_{in}. \tag{12}$$

Equation (12) indicates that Z_{in} can be adjusted with the proposed control. Therefore, it is proved that the proposed control can compensate for the impedance mismatch even though it is applied to the SBAR on the secondary side.

Fig. 10(a) shows the conceptual waveforms in which the system operates at the design point and the SBAR switches are in the off-state. As all the resonant parameters are in resonance, it is possible to reach the target battery voltage $V_{\text{batt,target}}$ using the β control, as shown in Fig. 10(b). As mentioned earlier, $Z_{o,ac}$ is resistive when the β control is applied to the SBAR.

When k becomes higher than $k_{\min}$, as shown in Fig. 11(a), the impedance mismatch occurs. Consequently, the output voltage gain is reduced, and it is impossible to reach $V_{\text{batt,target}}$ using only the β control, as shown in Fig. 11(b). As shown in Section III-C and Table II, $f_{\text{res}1}$ must be decreased, and $f_{\text{res}2}$ must be increased to compensate for the impedance mismatch when $k > k_{\min}$. Therefore, the proposed β and γ control is applied to the

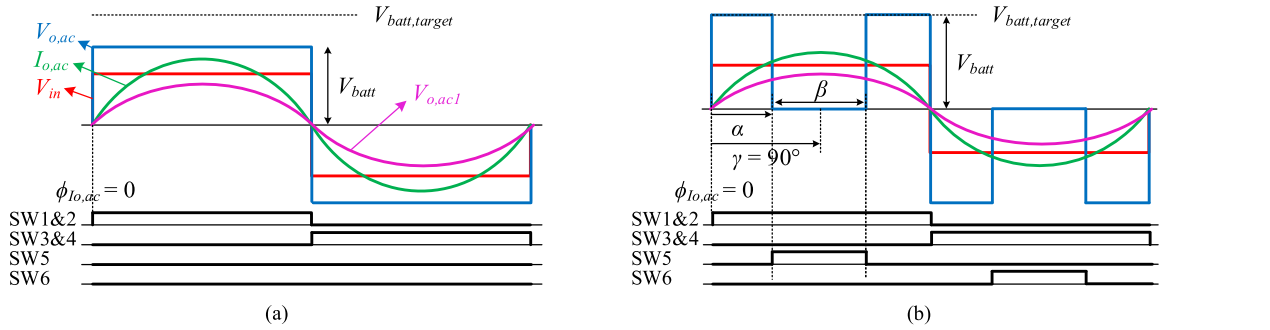

Fig. 10. Conceptual waveforms of the IPT system with the SBAR at the design point ($k = k_{\min}$). (a) Operation without SBAR control at the design point. (b) β control is applied to the SBAR at the design point (Resistive $Z_{o,ac}$).

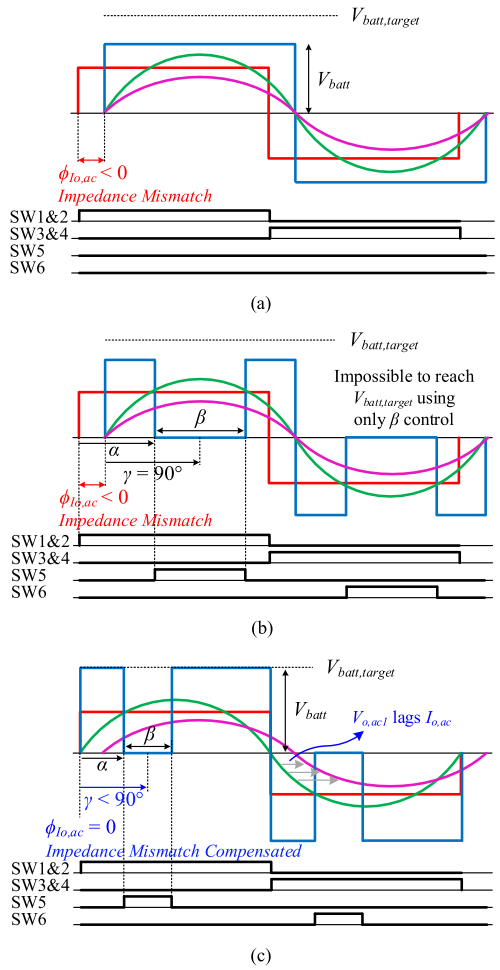

Fig. 11. Conceptual waveforms of the IPT system with the SBAR under the impedance mismatch condition due to the increase in k ($k > k_{\min}$). (a) Operation without SBAR control when $k > k_{\min}$. (b) β control when $k > k_{\min}$ (Resistive $Z_{o,ac}$). (c) β and γ control when $k > k_{\min}$ (Capacitive $Z_{o,ac}$).

SBAR for the impedance compensation, as shown in Fig. 11(c). When γ is controlled to be lower than 90°, $V_{o,ac1}$ lags $I_{o,ac}$ and the capacitive $Z_{o,ac}$ is implemented. In other words, the capacitive $Z_{o,ac}$ can compensate for the impedance mismatch due to the increase in k, based on (5) and (6).

Additionally, if k becomes lower than $k_{\min}$, impedance mismatch due to the decrease in k occurs, as shown in Fig. 12(a).

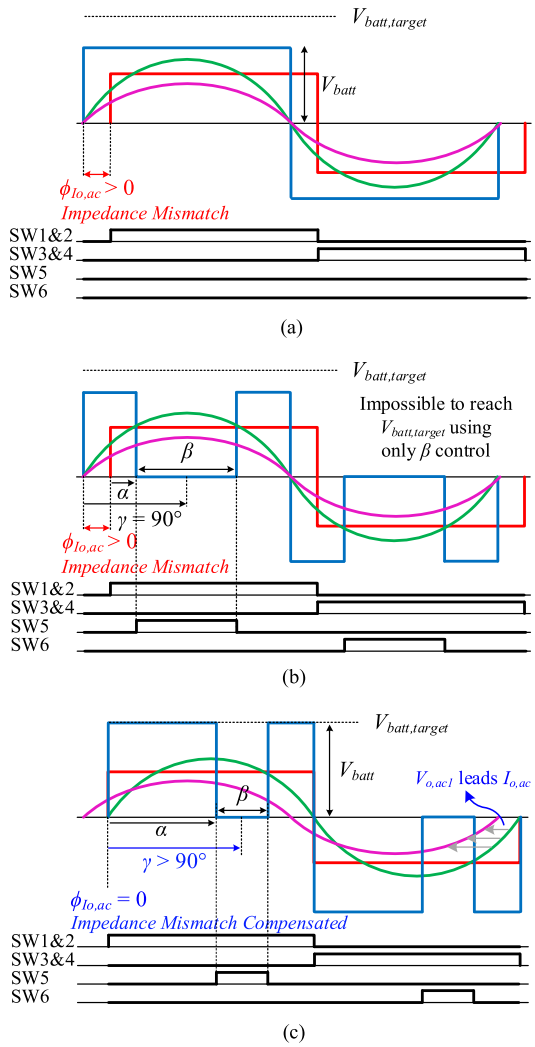

Fig. 12. Conceptual waveforms of the IPT system with the SBAR under the impedance mismatch condition due to the decrease in k ($k < k_{\min}$). (a) Operation without SBAR control when $k > k_{\min}$. (b) β control when $k < k_{\min}$ (Resistive $Z_{o,ac}$). (c) β and γ control when $k < k_{\min}$ (Inductive $Z_{o,ac}$).

Similar to Fig. 11(b), it is impossible to reach $V_{\mathrm{batt,target}}$ using only the β control, as shown in Fig. 12(b). In this case, $Z_{o,ac}$ should be inductively controlled to compensate for the impedance mismatch, as shown in Fig. 12(c).

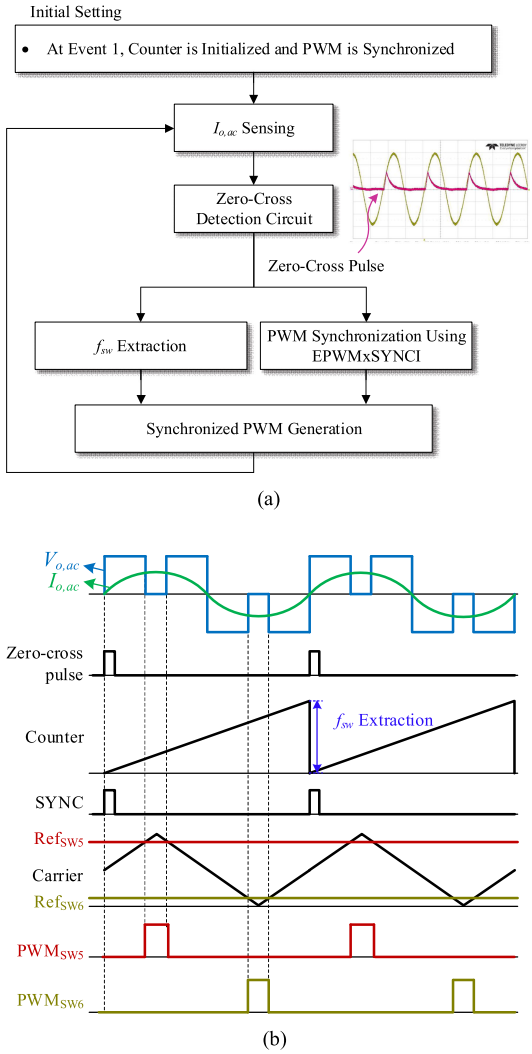

Fig. 13. Synchronous switching technique using the zero-crossing detection circuit. (a) Flowchart. (b) Control waveforms.

IV. Frequency Extraction and Synchronous Switching Technique

As the ZPA frequency tracking control is applied to the primary inverter to minimize the VA rating and to achieve a wide range of compensation, the secondary controller for the SBAR must be able to extract the primary switching frequency. In addition to frequency extraction, the SBAR must be synchronized with the primary inverter to compensate for the impedance mismatch by properly adjusting γ. Therefore, two methods for the frequency extraction and synchronous switching are proposed in this section using secondary information.

Fig. 13 shows a zero-crossing detection technique which detects a zero-crossing point of $I_{o,ac}$. The output of a current sensor for $I_{o,ac}$ is connected to a zero-crossing detection circuit, and a zero-crossing pulse is generated at the point when $I_{o,ac}$ moves into the positive half-cycle. When the rising edge is detected, a micro-control unit (MCU) starts to count and generates a PWM-synchronization signal. At the subsequent rising edge, the switching frequency f_{sw} is extracted from the counted value,

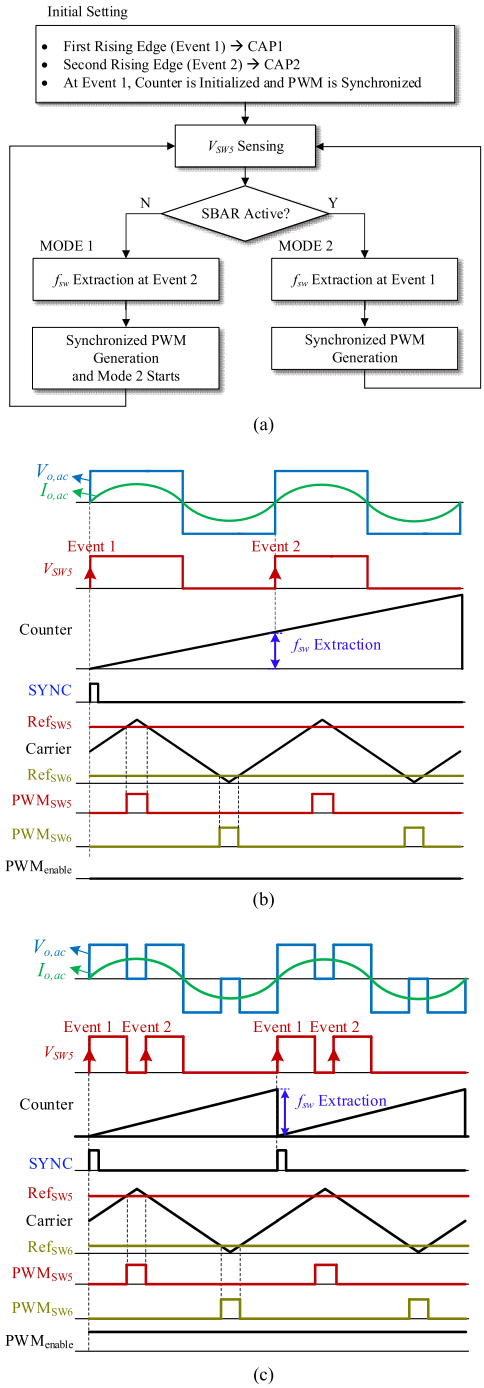

Fig. 14. Proposed synchronous switching technique using the rising edge detection of the switch voltage. (a) Flowchart. (b) Control waveforms (Mode 1: SBAR is not active). (c) Control waveforms (Mode 2: SBAR is active).

and the MCU initializes the counter. The zero-crossing detection circuit is well-known and simple to implement, but the additional current sensor with a wide bandwidth is essential; consequently, the cost of the system is increased.

To eliminate the additional current sensor, as shown in Fig. 14, a technique for detecting rising edge of the switch voltage V_{sw5} of the SBAR is proposed. The proposed method consists of two modes depending on whether the SBAR is inactive (Mode 1) or

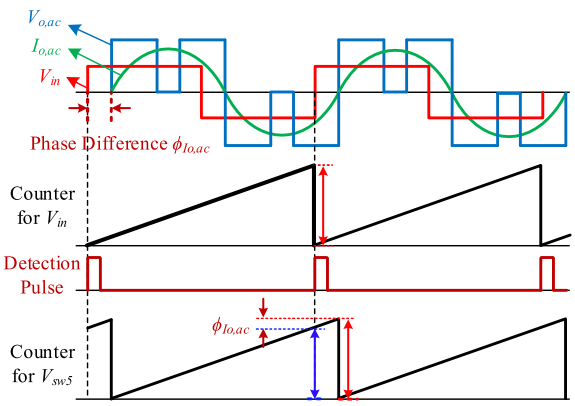

Fig. 15. Control waveforms of the $\phi_{Io,ac}$ detection control.

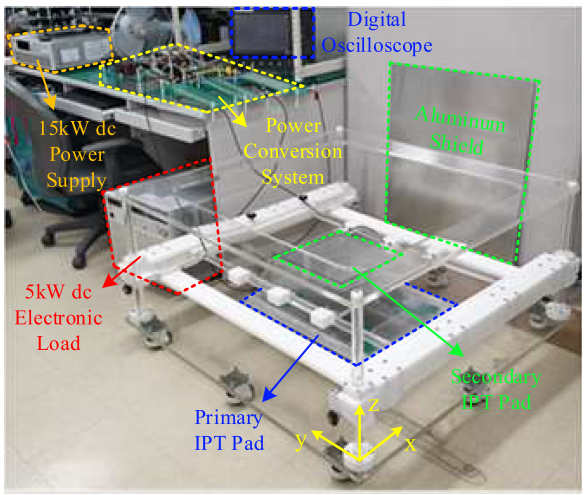

Fig. 16. Experimental setup of the IPT system with the SBAR.

TABLE III
DEVICE SPECIFICATIONS OF EXPERIMENTAL SETUP

Parameter	Description
MOSFET for primary inverter	IPW65R080CFD (650V / 43.3A)
MOSFET for SBAR	C3M0065090D (900V / 36A)
Diode for SBAR	IDW20G65C5 (650V / 20A)
Digital signal processor	TMS320F28335
Resonant capacitor	C1812C222JDGAC

TABLE IV
PARAMETERS OF THE RESONANT NETWORK

Constant parameter	Value		[Unit]
Input resonant inductor L_{in}	34.3		[μH]
Primary parallel capacitor C_p	102.6		[nF]
Primary filter capacitor C_f	8.302		[nF]
Secondary series capacitor C_s	46.51		[nF]
Variable parameter	k_{min}	k_{max}	[Unit]
Coupling coefficient k	0.09	0.21	-
Primary inductance L_p	460.6	441.1	[μH]
Secondary inductance L_s	77.11	80.07	[μH]

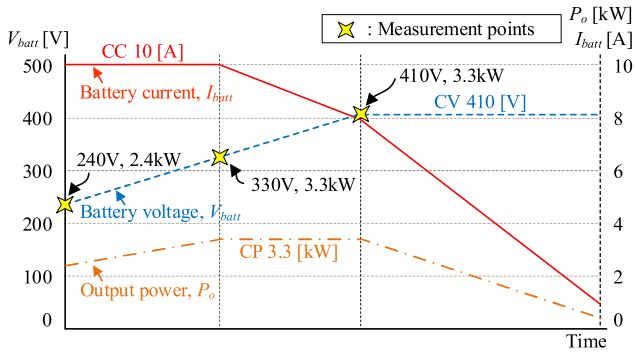

Fig. 17. Charging profile of the battery load and the efficiency-measurement points.

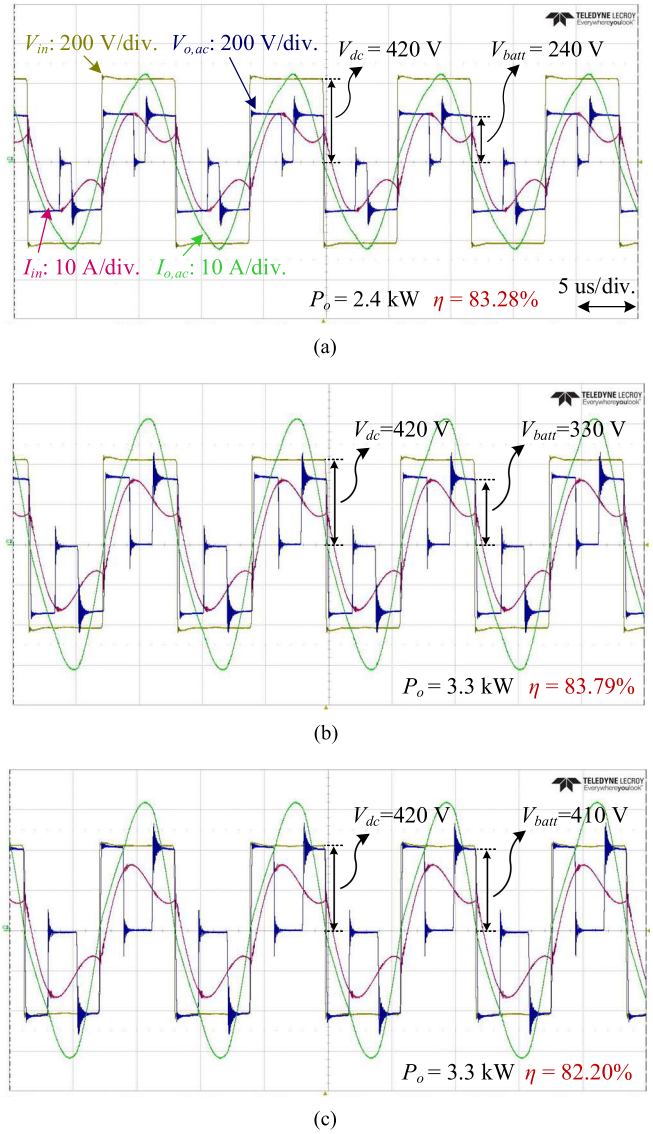

Fig. 18. Experimental waveforms of the SBAR according to V_{batt} at $k = k_{\mathrm{min}}$ in which only the duty control is applied to SBAR. (a) $V_{\mathrm{batt}} = 240$ V. (b) $V_{\mathrm{batt}} = 330$ V. (c) $V_{\mathrm{batt}} = 410$ V.

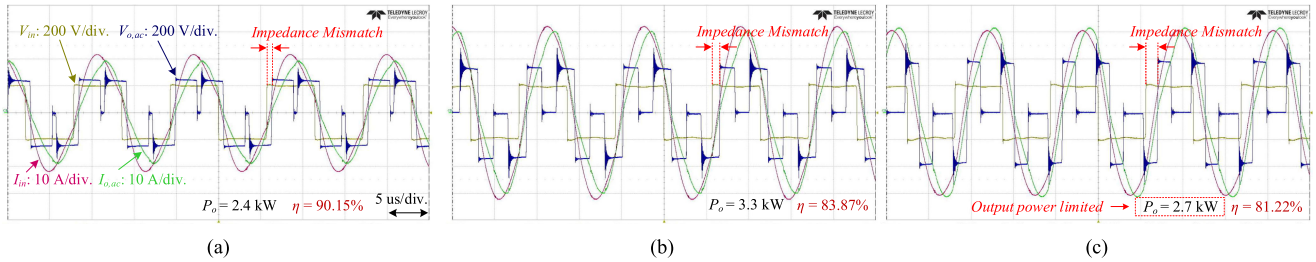

Fig. 19. Experimental waveforms of the SBAR according to $V_{\rm batt}$ at $k = k_{\rm max}$ in which only the duty control is applied to SBAR. (a) $V_{\rm batt} = 240$ V. (b) $V_{\rm batt} = 330$ V. (c) $V_{\rm batt} = 410$ V.

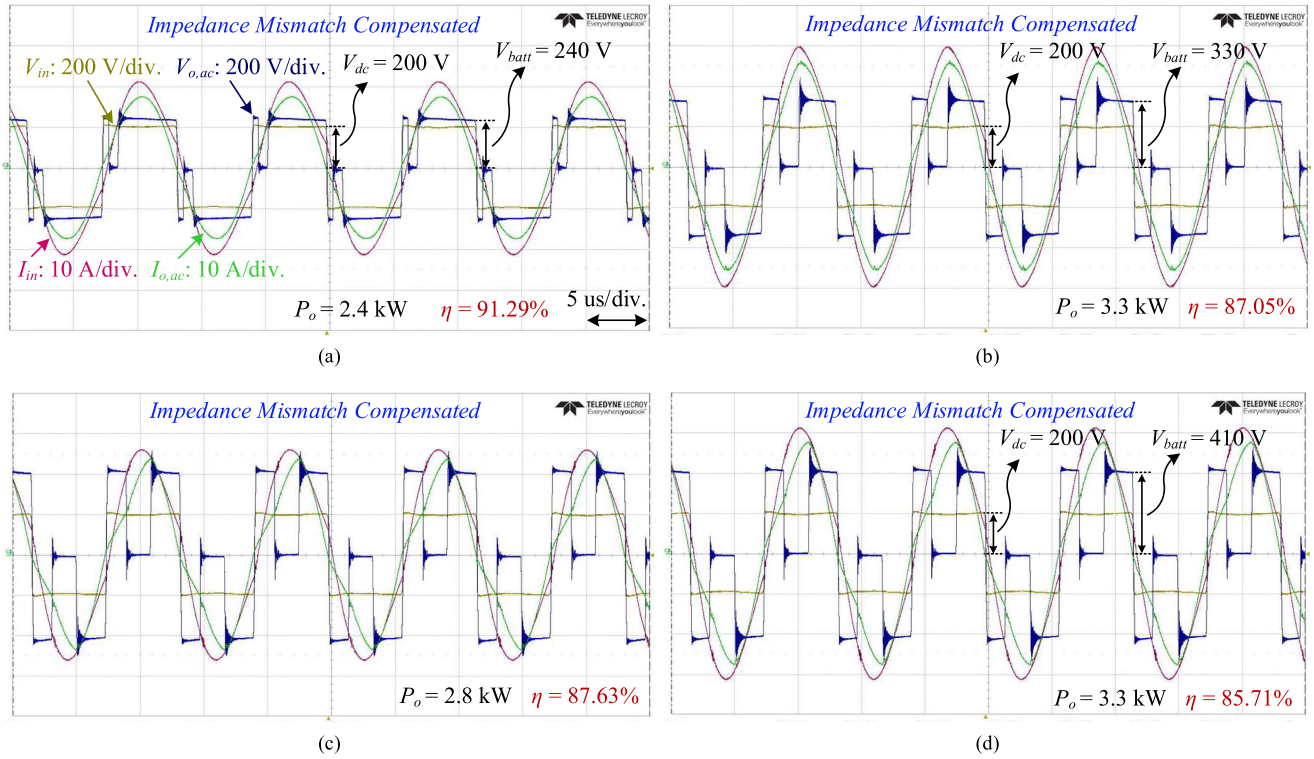

Fig. 20. Experimental waveforms of the SBAR according to $V_{\rm batt}$ at $k = k_{\rm max}$ in which the proposed control is applied to SBAR in order to compensate for the impedance mismatch. (a) $V_{\rm batt} = 240$ V. (b) $V_{\rm batt} = 330$ V. (c) $V_{\rm batt} = 410$ V. (d) $V_{\rm batt} = 410$ V.

active (Mode 2) because the rising edge of $V_{\rm sw\,5}$ appears once per period in Mode 1 and twice per period in Mode 2. The SBAR switches maintain the off state during Mode 1, which is a startup mode to extract $f_{\rm sw}$ before entering Mode 2. After extracting $f_{\rm sw}$, Mode 2 begins, and the SBAR is controlled. In both Modes 1 and 2, the MCU initializes the counter at the first rising edge (Event 1) and starts to count. At Event 1, the MCU generates the PWM-synchronization signal. In Mode 1, the time from the first to the second rising edge (Event 2) is one switching period of the SBAR. Thus, $f_{\rm sw}$ is extracted from the counted value at Event 2. By contrast, as the $V_{\rm sw\,5}$ rising events occur twice per period, $f_{\rm sw}$ is extracted from the counted value when Event 1 occurs again in Mode 2. Thus, even if the ZPA frequency tracking control is applied to the primary inverter, the $f_{\rm sw}$ of the SBAR can be extracted in real time without primary information or the current sensor. Once the $f_{\rm sw}$ is extracted, β is controlled through the output voltage feedback, and γ is controlled in an increasing or decreasing direction from 90° until the phase difference between V_{in} and $I_{o,ac}$ becomes zero. The phase difference $\phi_{Io,ac}$ is calculated using the difference between the counted values of V_{in} and $V_{\rm sw\,5}$ as shown in Fig. 15. It should be noted that the detection pulse is the only information received by the SBAR from the primary-side system [23]. Therefore, the proposed control can be implemented with minimal primary information.

V. Verification

A 3.3-kW prototype of the IPT system with the SBAR is manufactured to verify the proposed control, as shown in Fig. 16. The specifications of the experimental testbed are listed in Table III, and the parameters of the resonant network are listed in Table IV. As shown in Fig. 16, the dc link and the battery load are implemented using a 15-kW dc power supply and a 5-kW dc electronic load, respectively. In this article, the system

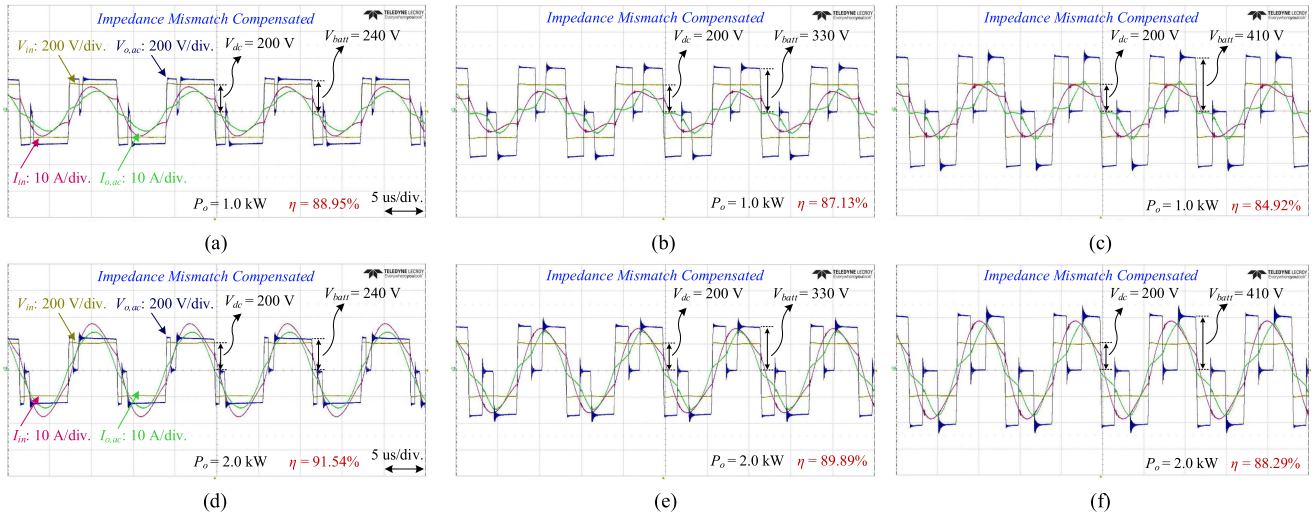

Fig. 21. Experimental waveforms of the SBAR according to $V_{\rm batt}$ and output power levels at $k = k_{\rm max}$. (a) $V_{\rm batt} = 240$ V, $P_o = 1$ kW. (b) $V_{\rm batt} = 330$ V, $P_o = 1$ kW. (c) $V_{\rm batt} = 410$ V, $P_o = 1$ kW. (d) $V_{\rm batt} = 240$ V, $P_o = 2$ kW. (e) $V_{\rm batt} = 330$ V, $P_o = 2$ kW. (f) $V_{\rm batt} = 410$ V, $P_o = 2$ kW.

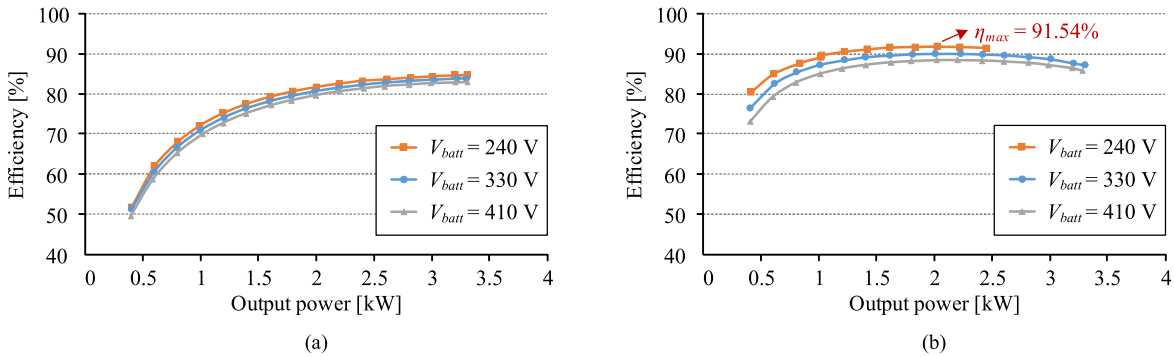

Fig. 22. Measured efficiency of the IPT system prototype with the SBAR according to $V_{\rm batt}$. (a) $k = k_{\rm min}$. (b) $k = k_{\rm max}$.

efficiency is measured from the dc power supply to the dc electronic load. Fig. 17 shows the charging profile of the battery load which has a 10 A CC charging region, 3.3 kW constant power (CP) charging region, and 410 V CV charging region. The proposed control is verified at the measurement points shown in Fig. 17.

A. Validation of Proposed Impedance Tuning

Fig. 18 shows the experimental waveforms at $k = k_{\rm min}$. In Fig. 18, impedance tuning is not required as $k_{\rm min}$ is the design point. Thus, it is possible to achieve the maximum output power of 3.3 kW even though only duty control is applied. However, as shown in Fig. 19, when the k condition is changed, the phase difference between V_{in} and $I_{o,ac}$ occurs because of the impedance mismatch. In addition, it is impossible to obtain the maximum output power of 3.3 kW when $k = k_{\rm max}$ and $V_{\rm batt} = 410$ V by applying only the duty control, as shown in Fig. 19(c). The proposed control is applied to the SBAR, as shown in Fig. 20, to compensate for the impedance mismatch. By applying the proposed control, $Z_{o,ac}$ is capacitively controlled, and the impedance mismatch is compensated. Consequently, it is possible to obtain the desired output power, and a maximum efficiency improvement of 6.4% is achieved at $P_o = 2.7$ kW. Moreover, the IPT system with the proposed control can achieve the maximum output power of 3.3 kW under the impedance mismatch, as shown in Fig. 20(d). In addition, Fig. 21 shows experimental waveforms of the proposed control according to different output power levels under the impedance mismatch condition. Through the experimental results, it is proved that the proposed control can improve the efficiency and expand the operable range of the system.

B. Efficiency and Loss Breakdown Analysis

As shown in Fig. 22, the efficiency is measured according to P_o and $V_{\rm batt}$ to evaluate the performance of the prototype and the proposed control. As shown in Fig. 22(b), a maximum efficiency of 91.54% is achieved with the proposed control when $k = k_{\rm max}$, $V_o = 240$ V, and $P_o = 2$ kW. As shown in Fig. 23, loss breakdown analysis is carried out to improve the efficiency of the proposed system. In Fig. 23, loss of antiparallel diode of the secondary MOSFET accounts for the largest portion of the total loss at $k = k_{\rm max}$. To reduce the antiparallel diode loss, an additional diode can be added to the secondary MOSFET. In addition, resonant capacitors can be more optimized because

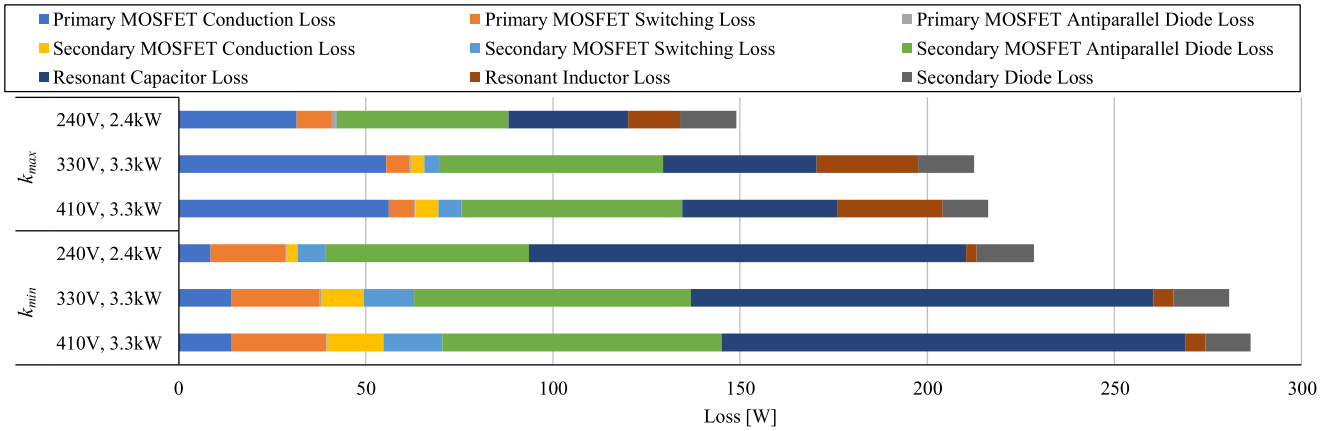

Fig. 23. Loss breakdown analysis of the IPT system prototype with the SBAR according to k conditions and output power levels.

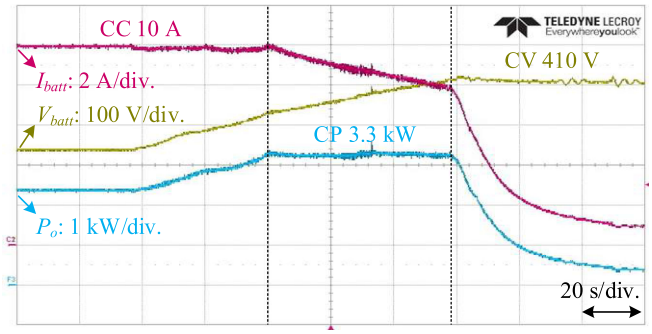

Fig. 24. CC-CP-CV charging curve of the SBAR with the proposed control under the impedance mismatch ($k = k_{\max}$).

many discrete capacitors are used in this prototype to facilitate manufacture.

C. Functional Verification

As shown in Fig. 24, according to the battery charging profile, the CC-CP-CV charging of the SBAR is verified with the proposed control under the impedance mismatch condition when $k = k_{\max}$.

VI. Conclusion

This article proposes an impedance tuning control for SBAR of an IPT system for EVs. The proposed control can compensate for the impedance mismatch caused by the misalignment of the IPT pads. The principle of the proposed impedance tuning is explained by analyzing the frequency characteristics and equivalent impedances, and the relationships between the turn-ON point, duty of the SBAR, and output equivalent impedance are derived. In addition, a technique for detecting voltage rising edge of the SBAR switch is proposed to extract the switching frequency of the SBAR and synchronize the SBAR with the primary-side system. A 3.3-kW IPT system prototype is manufactured to verify the proposed control. The validity and performance of the proposed control are verified through the experimental results.

References

[1] S. Li and C. C. Mi, "Wireless power transfer for electric vehicle applications," *IEEE J. Emerg. Sel. Top. Power Electron.*, vol. 3, no. 1, pp. 4–17, Mar. 2015.

[2] K. Aditya and S. S. Williamson, "Design considerations for loosely coupled inductive power transfer (IPT) system for electric vehicle battery charging - A comprehensive review," in *Proc. IEEE Transp. Electrific. Conf. Expo.*, 2014, pp. 1–6.

[3] R. Bosshard and J. W. Kolar, "Inductive power transfer for electric vehicle charging: Technical challenges and tradeoffs," *IEEE Power Electron. Mag.*, vol. 3, no. 3, pp. 22–30, Sep. 2016.

[4] SAE International. "Wireless power transfer for light-duty plug-in/electric vehicles and alignment methodology," 2017. [Online]. Available: http://standards.sae.org/wip/j2954/

[5] Qi Wireless Power Consortium. "The Qi wireless power transfer system power class 0 specification," 2016. [Online]. Available: https://www.wireless powerconsortium.com/knowledge-base/specifications/download-the-qi-specifications.html

[6] T. C. Beh, M. Kato, T. Imura, S. Oh, and Y. Hori, "Automated impedance matching system for robust wireless power transfer via magnetic resonance coupling," *IEEE Trans. Ind. Electron.*, vol. 60, no. 9, pp. 3689–3698, Sep. 2013.

[7] Y. Lim, H. Tang, S. Lim, and J. Park, "An adaptive impedance-matching network based on a novel capacitor matrix for wireless power transfer," *IEEE Trans. Power Electron.*, vol. 29, no. 8, pp. 4403–4413, Aug. 2014.

[8] A. Kamineni, G. A. Covic, and J. T. Boys, "Self-tuning power supply for inductive charging," *IEEE Trans. Power Electron.*, vol. 32, no. 5, pp. 3467–3479, May 2017.

[9] J. Kim, D. Kim, and Y. Park, "Free-positioning wireless power transfer to multiple devices using a planar transmitting coil and switchable impedance matching networks," *IEEE Trans. Microw. Theory Techn.*, vol. 64, no. 11, pp. 3714–3722, Nov. 2016.

[10] A. Kamineni, M. J. Neath, G. A. Covic, and J. T. Boys, "A mistuning-tolerant and controllable power supply for roadway wireless power systems," *IEEE Trans. Power Electron.*, vol. 32, no. 9, pp. 6689–6699, Sep. 2017.

[11] D. Kim and D. Ahn, "Self-tuning LCC inverter using PWM-controlled switched capacitor for inductive wireless power transfer," *IEEE Trans. Ind. Electron.*, vol. 66, no. 5, pp. 3983–3992, May 2019.

[12] R. W. Porto, V. J. Brusamarello, L. A. Pereira, and F. R. de Sousa, "Fine tuning of an inductive link through a voltage-controlled capacitance," *IEEE Trans. Power Electron.*, vol. 32, no. 5, pp. 4115–4124, May 2017.

[13] A. Trigui, S. Hached, F. Mounaim, A. C. Ammari, and M. Sawan, "Inductive power transfer system with self-calibrated primary resonant frequency," *IEEE Trans. Power Electron.*, vol. 30, no. 11, pp. 6078–6087, Nov. 2015.

[14] G. R. Kalra, B. S. Riar, and D. J. Thrimawithana, "An integrated boost active bridge based secondary inductive power transfer converter," *IEEE Trans. Power Electron.*, vol. 35, no. 12, pp. 12716–12727, Dec. 2020.

[15] R. Mai, Y. Liu, Y. Li, P. Yue, G. Cao, and Z. He, "An active-rectifier-based maximum efficiency tracking method using an additional measurement coil for wireless power transfer," *IEEE Trans. Power Electron.*, vol. 33, no. 1, pp. 716–728, Jan. 2018.
[16] K. Colak, E. Asa, M. Bojarski, D. Czarkowski, and O. C. Onar, "A novel phase-shift control of semibridgeless active rectifier for wireless power transfer," *IEEE Trans. Power Electron.*, vol. 30, no. 11, pp. 6288–6297, Nov. 2015.
[17] X. Zhang *et al.*, "A control strategy for efficiency optimization and wide ZVS operation range in bidirectional inductive power transfer system," *IEEE Trans. Ind. Electron.*, vol. 66, no. 8, pp. 5958–5969, Aug. 2019.
[18] Y. Liu, U. K. Madawala, R. Mai, and Z. He, "An optimal multivariable control strategy for inductive power transfer systems to improve efficiency," *IEEE Trans. Power Electron.*, vol. 35, no. 9, pp. 8998–9010, Sep. 2020.
[19] M. Kim, D. Joo, and B. K. Lee, "Design and control of inductive power transfer system for electric vehicles considering wide variation of output voltage and coupling coefficient," *IEEE Trans. Power Electron.*, vol. 34, no. 2, pp. 1197–1208, Feb. 2019.
[20] M. Kim, D. Joo, and B. K. Lee, "High efficient power conversion circuit for inductive power transfer charger in electric vehicles," in *Proc. IEEE 3rd Int. Future Energy Electron. Conf. ECCE Asia*, 2017, pp. 25–29.
[21] S. Ann, W. Son, J. Byun, J. H. Lee, and B. K. Lee, "Switch design for a high-speed switching semi-bridgeless active rectifier of inductive power transfer systems considering reverse recovery phenomenon," in *Proc. 10th Int. Conf. Power Electronics ECCE Asia*, 2019, pp. 1–6.
[22] C. Wang, G. A. Covic, and O. H. Stielau, "Power transfer capability and bifurcation phenomena of loosely coupled inductive power transfer systems," *IEEE Trans. Ind. Electron.*, vol. 51, no. 1, pp. 148–157, Feb. 2004.
[23] S. Ann, J. Byun, W. J. Son, J. H. Lee, and B. K. Lee, "Impedance tuning control and synchronization technique for semi-bridgeless active rectifier of IPT system in EV applications," in *Proc. IEEE Appl. Power Electron. Conf. Expo.*, 2020, pp. 1622–1626.

Sangjoon Ann (Student Member, IEEE) received the B.S. degree in electrical engineering in 2016 from Sungkyunkwan University, Suwon, South Korea, where he is currently working toward the combined M.S. and Ph.D. degree in electrical and computer engineering.

His research interests include wireless power transfer, wide bandgap semiconductor devices, and resonant converters.

Byoung Kuk Lee (Senior Member, IEEE) received the B.S. and the M.S. degrees from Hanyang University, Seoul, South Korea, in 1994 and 1996, respectively, and the Ph.D. degree from Texas A&M University, College Station, TX, USA, in 2001, all in electrical engineering.

From 2003 to 2005, he was a Senior Researcher with Power Electronics Group, Korea Electrotechnology Research Institute, Changwon, South Korea. Since 2006, he has been working with the College of Information and Communication Engineering, Sungkyunkwan University, Suwon-si, South Korea. His research interests include on-board chargers and wireless power transfer chargers for electric vehicles, battery management system algorithms, energy storage systems, hybrid renewable energy systems, dc distribution systems for home appliances, modeling and simulation, and power electronics.

Dr. Lee was a recipient of the Outstanding Scientists of the 21st Century from IBC and was listed on the 2008 edition of Who's Who in America and the 2009 edition of Who's Who in the World. He is a Guest Associate Editor for the IEEE TRANSACTIONS ON POWER ELECTRONICS and an Associate Editor for the IEEE TRANSACTIONS ON TRANSPORTATION ELECTRIFICATION. He was the Presenter for the Professional Education Seminar on-board charger technology for EVs and PHEVs at the IEEE Applied Power Electronics Conference in 2014. He was the General Chair for the IEEE Vehicular Power and Propulsion Conference in 2012. Since 2016, he has been a member of the IEC Conformity Assessment Board.